10

Quantitative Analysis of Biological Cells Using Digital Holographic Microscopy

Natan T. Shaked, Lisa L. Satterwhite, Matthew T. Rinehart and Adam Wax
Department of Biomedical Engineering, Fitzpatrick Institute for Photonics, Duke University, Durham, North Carolina 27708, USA

1. Introduction

Biological cells are microscopic dynamic objects, continuously adjusting their three-dimensional sizes, shapes and other biophysical features. Wide-field microscopy of cell dynamics can provide a powerful research tool for cell biology studies, as well as a potential means for medical diagnosis and monitoring of diseases. Biological cells, however, are mostly-transparent objects, and thus imaging them with conventional intensity-based light microscopy fails to provide adequate optical contrast between the cell and its environment. Although exogenous contrast agents such as fluorescent dyes can be used to solve this problem, they might be cytotoxic in the long run and there is a possibility they will influence the cellular behavior. Additionally, fluorescent dyes tend to photobleach, potentially limiting the imaging time.

The contrast problem when imaging biological cells can also be solved by using phase microscopy, which records the optical path delays of light passing through the cells and subsequently obtains information on the cellular structure and dynamics without using any exogenous labelling. Since detectors are sensitive to intensity only, the phase of the light that has interacted with the cells must first be converted to intensity variations for detection. Widely used methods to achieve this include phase contrast microscopy and differential interference contrast (DIC) microscopy. However, these techniques are not inherently quantitative and present distinct imaging artifacts that typically prevent straightforward extraction of the entire optical path delay profile of the cell.

Wide-field digital interferometry (WFDI) is a label-free holographic technique that is able to record the entire complex wavefront (amplitude and phase) of the light which has interacted with the sample (Cuche et al., 1999). From the recorded complex field, one can obtain full quantitative phase profiles of cells as well as correct for out-of-focus image features by post-processing. WFDI microscopy (also called digital holographic microscopy) has been applied to various types of biological cell systems and has recorded a diverse range of cellular phenomena (Marquet et al., 2005; Ikeda et al., 2005; Shaked et al., 2009 b; Shaked et al., 2010 b-d). Section 2 reviews the principle of WFDI for obtaining phase profiles of cells, starting from the experimental setup, and ending in digital processing for obtaining the final quantitative phase profile of the cell.

Although WFDI is a quantitative recording technique, simple quasi-three-dimensional holographic visualization of the cell phase profile need not be the end of the process.

Quantitative analysis should permit extraction of numerical parameters which are useful for cytology or medical diagnosis. Using a transmission-mode interferometric setup, the resulting phase profile represents the multiplication between the refractive index differences and the thickness of the sample. These coupled parameters, the refractive index and the thickness, are not distinct when acquiring the phase profile of a dynamic cell. To allow quantitative cell analysis by WFDI, this fact must be considered during the system development and the following quantitative data analysis. Section 3 first deals with the interpretation of the resulting phase profile of the cell. As also reviewed in this section, many morphological parameters that are useful for cell biologists (such as cell volume, cell force distribution, etc.) are based on the geometric thickness profile of the cell rather than on its phase profile. Therefore, we review methods to decouple the cell thickness from refractive index using the cell phase profile obtained by WFDI. As will be shown, for certain cells, in which a constant refractive index can be assumed for the entire cell contents, such as red blood cells, the thickness profile can be directly obtained from the phase profile. In contrast, for other types of cells containing inner organelles with different refractive indices (e.g. nuclei, mitochondria, etc.), certain parameters such as area, dry-mass, and relative volume can still be calculated directly from the phase profile. Measurements of these parameters are presented for experiments with articular cartilage chondrocytes. If, however, a complete thickness profile is required, more complex experimental measurements are typically employed. Decoupling cell refractive index and thickness can be accomplished, for example, by measuring the phase profiles of the same cell immersed in two different growth media with distinct refractive indices. Alternatively, when the thickness profile is measured by another method (such as confocal microscopy), it is possible to use WFDI to calculate the refractive index of the cell inner organelles.

Finally, we show in Section 4 that the phase profile is still useful for quantitative analysis of cells even in cases where decoupling of thickness and refractive index is not possible or desired. This operation is carried out by defining new numerical phase-profile-based parameters, which can characterize certain cell processes of value to cell biologists. Experimental demonstrations of this approach will be presented using cardiomyocytes (heart muscle cells) undergoing temperature changes. These cells contain a significant number of subcellular organelles with varying refractive indices. In addition, the cell dynamics are characterized by a rapid contraction of the cell followed by restoration to the resting point. Capturing the dynamics of these cells during tremperature change by measuring the phase profiles with WFDI is shown to be a suitable method for obtaining quantitative parameters for biological studies, even without the need for decoupling cell thickness from refractive index.

2. Acquiring the phase profile of biological cells by WFDI

Figure 1(a) presents a possible scheme of a single-exposure WFDI setup that is based on the Mach-Zehnder interferometer and an off-axis holographic geometry. In this optical setup, light from a coherent source (HeNe laser, for example) is first spatially filtered using a pair of spherical lenses and a confocally-positioned pinhole, and then split into reference and object beams by beam splitter BS_1. The object beam is transmitted through the sample and magnified by a microscope objective. The reference beam is transmitted through a compensating microscope objective (typically similar to the object-beam objective) and then

combined with the object beam at an angle. The combined beams are projected onto a digital camera by lens L_2, which is postioned in a 4f configuration with each of the microscope objectives, meaning that the distance between each of the microscope objectives and lens L_2 is equal to the summation of their focal lengths. This configuration allows projection of the amplitude and phase distribution of the sample onto the camera. The combination of the sample and reference beams creates a high spatial frequency off-axis hologram of the sample on the digital camera. The digital off-axis hologram acquired by the camera is the intensity of the summation of the object and reference waves, and can be mathematically expressed as follows:

$$H(x,y) = \left|E_s + E_r\right|^2 = \left|E_s\right|^2 + \left|E_r\right|^2 + \left|E_s\right|\left|E_r^*\right|\exp[j(\phi(x,y) + qx)], \tag{1}$$

where E_s and E_r are respectively the sample and reference field distributions, $\phi(x,y)$ is the spatially-varying phase associated with the sample, q is the fringe frequency due to the angular shift between the sample and reference fields, x is the direction of the angular shift (assuming linear horizontal fringes in the off-axis hologram).

The common digital processing method applied to the off-axis hologram starts with a digital two-dimensional Fourier transform. The resulting spatial-frequency contents include reference-field and sample-field autocorrelations (as a result of transforming the first two elements of Eq. (1)) that are located around the origin of the spatial spectrum, and two mathematically conjugated cross-correlation terms (as a result of transforming the exponential term in Eq. (1)), each located at a different side of the spatial spectrum. The exact locations of the cross-correlation terms are dependent on the angle between the object and reference beams. Looking at the spectrum profile, it is easy to isolate only one of the cross-correlation terms, center it, and perform a digital two-dimensional inverse Fourier transform on the result, yielding $\left|E_s\right|\left|E_r^*\right|\exp[j(\phi(x,y)]$. Assuming a weak amplitude modulation due to the transparancy of biological cells in culture, the phase argument of the result $\phi(x,y)$ is the phase profile of the sample.

An alternative method for isolating the phase $\phi(x,y)$ is to perform digital spatial filtering in the image domain rather than in the spectral domain; this is easy to implement automatically, even for dynamic samples (Shaked et al., 2009 a; Shaked et al., 2010 d). Assuming a linear horizontal fringe pattern, the background fringe frequency q in Eq. (1) can be calculated by summing the fringe pattern columns of a small part of the background and fitting the resulting vector to a sine wave. Then, Eq. (1) should be digitally multiplied by $\exp(-jqx)$, and $(\left|E_r\right|^2 + \left|E_s\right|^2)\exp(-jqx)$ can be removed by measuring $\left|E_r\right|^2$ and $\left|E_s\right|^2$, or, if the sample is dynamic, it is possible to simply remove only high spatial frequencies until the optimal result for the phase profile is obtained.

To understand the meaning of the measured phase profile, let us look at Figure 1(b), which presents the sample chamber in detail. As can be seen in this image, the *in vitro* cell is typically adhered to the bottom coverslip and is immersed in cell growth medium. The top coverslip of the chamber ensures a constant cell medium height accross the chamber and thus a constant physical chamber thickness. Based on this chamber, the spatially-varying phase measured by WFDI is proportional to the optical path delay (OPD) profile of the sample and defined as follows:

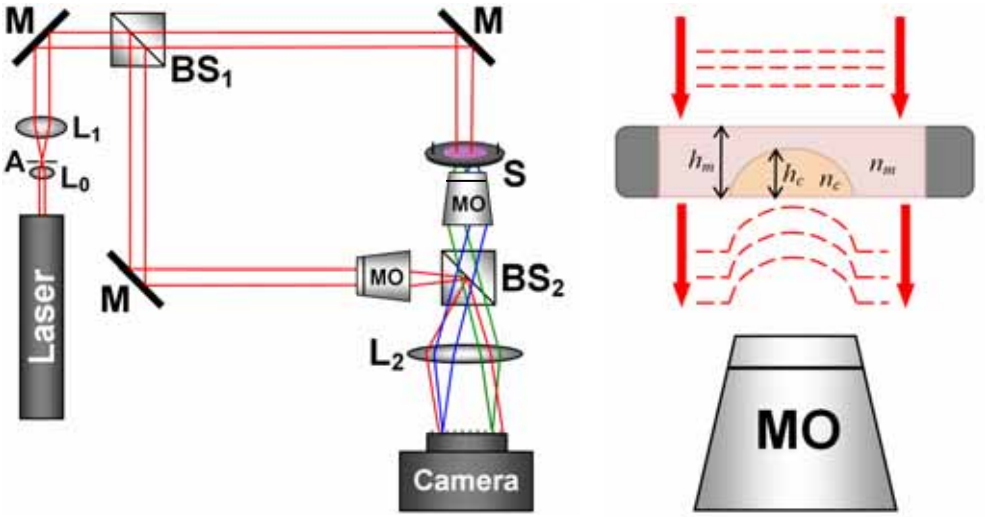

(a) (b)

Fig. 1. (a) Off-axis WFDI phase-microscopy system. A = Pinhole; L_0, L_1, L_2 = Lenses; BS_1, BS_2 = Beam splitters; M = Mirror; S = Sample; MO = Microscope objective; (b) Detailed scheme of the sample chamber.

$$\begin{aligned}\phi(x,y) &= \frac{2\pi}{\lambda}\left[\bar{n}_c(x,y)h_c(x,y) + n_m\left(h_m - h_c(x,y)\right)\right] \\ &= \frac{2\pi}{\lambda}\left[\left(\bar{n}_c(x,y) - n_m\right)h_c(x,y) + n_m h_m\right] \\ &= \frac{2\pi}{\lambda}\left[OPD_c(x,y) + OPD_m\right],\end{aligned} \tag{2}$$

where λ is the illumination wavelength, $\bar{n}_c(x,y)$ is the spatially varying integral refrative index, n_m is the medium refractive index, $h_c(x,y)$ is the spatially varying thickness profile of the cell, and h_m is the height of the cell medium. For each spatial point (x,y), the integral refrative index $\bar{n}_c$ is defined as follows (Rappaz et al., 2005):

$$\bar{n}_c = \frac{1}{h_c}\int_0^{h_c} n_c(z)dz, \tag{3}$$

where $n_c(z)$ is a function representing the intracellular refractive index along the cell thickness. The value of $OPD_m = n_m h_m$ can be measured in advance in places where there are no cells located, and then subtracted from the total OPD measurement. However, $OPD_c = \left(\bar{n}_c(x,y) - n_m\right)h_c(x,y)$ contains two coupled parameters: the integral refractive index profile of the cell and the cell thickness profile (under the assumption that n_m is known). These parameters might not be distinct when acquiring the phase profile of a dynamic cell, and this fact must be considered during development of the WFDI optical system capturing the cell phase profile and in the quantitative data analysis that follows. Local changes in the cell refractive index along the cell thickness may occur during various dynamic processes,

such as action potential propagation, or by transverse movement of the inner organelles of the cell. Independently or not, thickness changes can occur due to any morphological change of the cell such as membrane fluctuations and cell swelling.

3. Thickness – refractive index conjugation in the phase profile

Various morphological parameters that are useful for cell biologists, including cell volume and cell force distribution, are based on the thickness profile of the cell rather than on the phase profile. Many methods have been developed to decouple thickness from refractive index difference using the cell phase profile. Popescu et al. (2005, 2008 a) and Rappaz et al. (2008 a) have shown that for certain cells, such as mature red blood cells, in which a constant refractive index can be assumed for the entire cell contents (e.g. $\overline{n}_c \cong 1.395$), the thickness profile can be directly obtained from the phase profile. Since WFDI is able to record the quantitative thickness profile of the red blood cell, it is possible to measure rapid height changes, such as membrane fluctuations, that can indicate various medical conditions and blood diseases (Park et al., 2008; Park et al., 2010). Figure 2 shows the phase profiles of rat red blood cells obtained by WFDI in our laboratory, and the associated thickness profile for an arbirary cell in the field of view (FOV). Note, however, that this method of decoupling cell thickness from refractive index in WFDI-base phase profiles is limited to homogeneous cell types that do not contain nuclei or other organelles with varying refractive indices.
Other studies (Barer, 1952; Popescu et al., 2008 b; Rappaz et al., 2009) have shown that for heterogeneous cells that contain organelles with different refractive indices, certain parameters such as cell area and dry mass can be obtained directly from the phase profile. Cell area S_c is simply defined as the number of pixels, for which the OPD is above the background OPD, multiplied by the pixel area. After S_c is known, cell dry mass can be calculated by the following formula:

$$M = \frac{1}{\alpha}\int_{S_c} OPD_c(x,y)ds = \frac{S_c}{\alpha}\langle OPD_c \rangle, \tag{4}$$

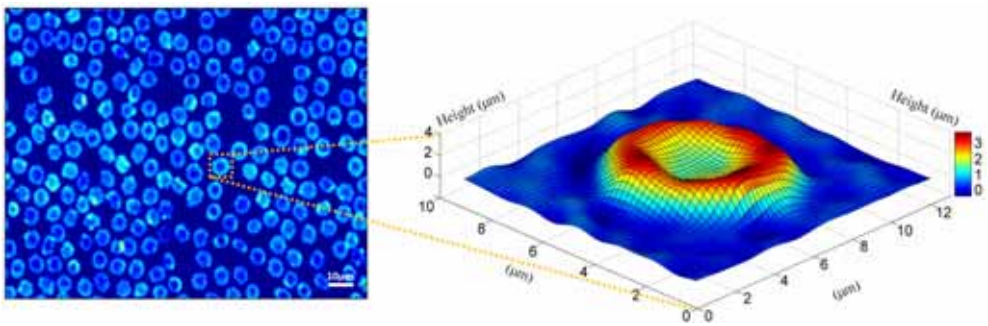

Fig. 2. WFDI-based phase profile of rat whole blood under 40x magnification, demonstrating the valuable quantitative morphological data that can be obtained by WFDI in a single exposure, and without any type of sample preparation or labeling. Cell height profile is shown on the right. This quantitative profile can be derived for each of the cells in the FOV.

where α is the refractive increment constant and can be approximated as 0.18-0.21 ml/g (Barer, 1952), and where $\langle OPD_c \rangle$ is the average OPD over the entire cell area. In a similar way, dry mass surface density can be calculated as follows:

$$\sigma_M(x,y) = \frac{1}{\alpha} OPD_c(x,y) . \quad (5)$$

In addition, if the cell volume transiently increases in an isotropic way (for example, due to swelling), relative volume can still be calculated in a good approximation. For example, we have shown that cell swelling in articular chondrocytes can be analyzed quantitatively without the need to decouple the thickness from refractive index in the WFDI-based phase measurement (Shaked et al., 2010 d). Articular chondrocytes are the cells that compose the cartilage, the connective tissue that distributes mechanical loads between bones and provides almost frictionless surfaces in the joints. The phenotypic expression and metabolic activity of these cells are strongly influenced by shape and volume changes occurring due to mechanical and osmotic stresses. Chondrocytes exhibit rapid swelling or shrinking followed by an active volume recovery in response to osmotic stress. Thus instantaneous evaluation of the chondrocyte volumetric adaptation to such stresses can provide important information on the structure–function relationships in these cells. We induced hypoosmotic stress on *in vitro* chondrocytes by changing the cell medium (Shaked et al., 2010 d). Due to the stress, the cells started swelling and ultimately burst. We recorded the dyanmic phase profiles of the chondrocytes during this phenomenon by WFDI. Figure 3(a) shows the phase profile of one chondrocyte in the monolayer at three different time points. During cell swelling, the phase profile looks wider and lower. Figure 3(b) shows a two-dimensional view of the phase profiles of several cells in the monolayer, whereas Fig. 3(c) shows a DIC microscopy image of the sample. This demonstrates that the contrast mechanism in DIC microscopy does not yield quantitative information while the contrast in WFDI allows direct quantification of the OPD and various numerical parameters at each spatial point on the cell. In addition, as we have shown (Shaked et al., 2010 d), since WFDI captures the entire wavefront, it is possible to correct for out of focus effects in the sample using only digital Fresnel propagation in post-processing and thus avoiding mechanical sample adjustment. This cannot be accomplished using a non-quantitative technqiue such as DIC microscopy.

Based on these dynamic quantitative WFDI-based phase profiles, we calculated relative volume (according to methods described by Popescu et al. (2008 b) and based on the assumption of isotropic volume change); relative dry mass according to Eq. (4); relative area; and relative average phase. All parameters were calculated as the fractional change from the initial value. Figure 3(d) presents the temporal changes of these parameters during the single-cell hypoosmotic swelling (for the cell illustrated in Fig. 3(a)). As can be seen from these graphs, the chondrocyte volume and area increased by 46% and 52%, respectively, during swelling and maintained an approximately constant dry mass. Figure 3(e) shows the parameter graphs for the hypoosmotic swelling of another single chondrocyte that gained in volume and area until bursting, at which point its dry mass decreased. This observation provides experimental support of the dry mass calculation (Eq. (4)) that is based on the chondrocyte phase profile. The small jumps that can be seen on the graphs before the chondrocyte bursts are further validation of Eq. (4). These jumps correspond exactly to time points at which intracellular debris from other previously burst chondrocytes enter the field of view (FOV). Based on the high temporal resolution of our measurements, we have calculated the chondrocyte volume just prior to bursting as V_L=1.28 times the initial cell

volume V_0. Figure 3(f) shows the time dependence of the relative area, dry mass, and average phase of the cell monolayer visualized in Fig. 3(b). The graphs illustrate the trends in these parameters that occur during the dynamic response of the monolayer. Different chondrocytes start swelling at different time points, swell to various extents, and burst at different time points. Individual cell swelling and bursting results in a decrease in the average phase value. The rupture of an individual cell is characterized by a loss of dry mass and an increase of viewable area until the chondrocyte intracellular debris leaves the FOV. New chondrocytes and intracellular debris entering the FOV result in an increase in dry mass and area. It was demonstrated that the values of all three parameters decrease over time due to the rupture of most chondrocytes in the monolayer; this results in an approximately uniform distribution of intracellular debris in the chamber (Shaked et al., 2010 d).

Note that in the chondrocyte experiment, we did not decouple thickness from refractive index since the calculated parameters did not require this operation. If, however, a complete thickness profile is required, more involved experimental measurements are typically employed. Rappaz et al. (2008 a, 2009) used two types of cell media with distinct refractive indices and measured two phase profiles of the same cell. The cell is first measured in the presence of a cell medium with refractive index n_m , yielding a measured cellular OPD of:

$$OPD_{c,1}(x,y) = \left(\bar{n}_c(x,y) - n_m\right) \cdot h_c(x,y). \tag{6}$$

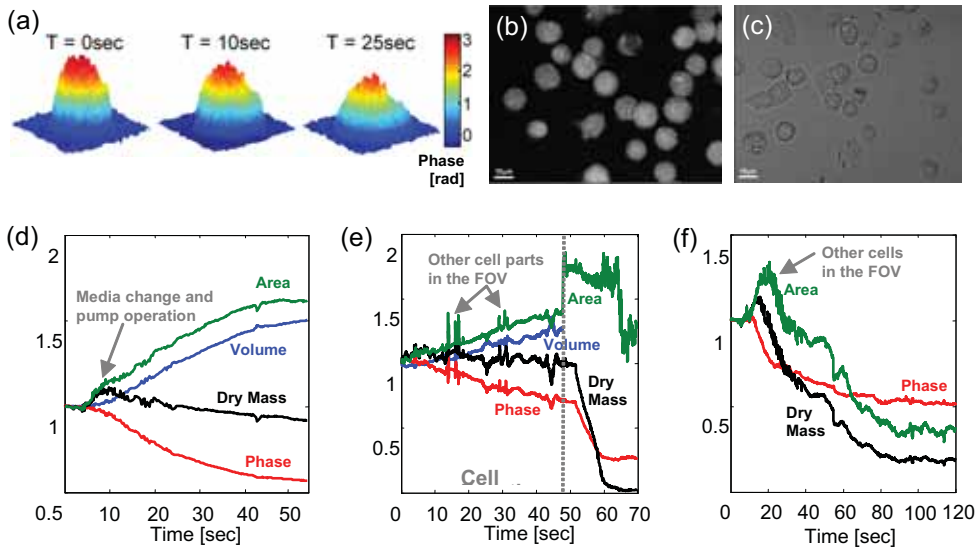

Fig. 3. Articular chondrocyte fast dynamics due to hypoosmotic pressure: (a) WFDI-based surface plots of the phase profiles at several different time points; (b) WFDI-based phase profile of the cell monolayer, acquired at 120 frames per second; (c) Phase image of the monolayer obtained by DIC microscopy. (d)-(f) WFDI-based graphs of the relative change in various cell morphological parameters during: (d) single-cell swelling as partially visualized in (a); (e) single-cell swelling and bursting; and (f) cell monolayer dynamics as partially visualized in (b). (Shaked et al., 2010 d).

Then, the current cell medium is replaced by another medium with the same osmolarity, to avoid cell volume changes, but with a different refractive index of $n_m + \Delta n$, yielding a cell OPD of:

$$OPD_{c,2}(x,y) = \left(\overline{n}_c(x,y) - \left(n_m + \Delta n_m\right)\right) \cdot h_c(x,y). \tag{7}$$

The cell thickness profile can be obtained by subtracting Eqs. (6) and (7) which yields:

$$h_c(x,y) = \frac{OPD_{c,1}(x,y) - OPD_{c,2}(x,y)}{\Delta n_m}. \tag{8}$$

Substituting Eq. (8) in Eq. (6) and (7) yields the integral refractive index of the cell as follows:

$$\overline{n}_c(x,y) = \frac{OPD_{c,1}(x,y)\Delta n_m}{OPD_{c,1}(x,y) - OPD_{c,2}(x,y)} + n_m. \tag{9}$$

Despite the simplicity of this two-exposure method, it is effective only if the cell is not highly dynamic and the changes between the consecutive phase measurements are minimal. In other cases, this method is not useful for measuring the correct thickness profile of the cell.

Alternatively, methods of scanning the cell from different points of view can be employed to obtain an intracellular refractive index map (Charrière et al. 2006, Choi et al., 2007). Briefly, phase profiles of the cell are measured by WFDI at different angles, by either rotating the sample or changing the illumination direction, and are then processed by a tomographic algorithm (e.g. the filtered backprojection algorithm) to obtain a three-dimensional refractive index map $n_c(x,y,z)$ of the cell. Since the obtained refractive index map is three-dimensional and not only the integral refractive index $\overline{n}_c(x,y)$ across a plane of view, it can be presented slice by slice using any pair of dimensions. This method is more complicated than simple WFDI, since it typically requires mechanical scanning with dedicated hardware, and it also assumes that the cell is static during the scan time; this precludes acquiring three-dimensional refractive index maps of highly dynamic cells.

Park et al. (2006) have proposed a system integrating WFDI and epi-fluorescence microscopy, which can in principle detect organelle locations in real time. If the organelle refractive indices and sizes are known in advance, then the cell thickness profile can be calculated. Rappaz et al. (2008 b) have proposed simultaneous measurement of cell thickness and refractive index by using two illumination wavelengths and a dispersive extracellular dye in the medium.

Alternatively, phase profile measurements can be used in a complementary way: rather than measuring or assuming a certain refractive index and calculating the cell thickness profile, the cell thickness can be measured by another method and then used in combination with the phase measurement obtained by WFDI to calculate the refractive indices of cellular organelles. For example, confocal microscopy has been used in combination with WFDI microscopy to measure refractive indices of cell organelles (Curl et al., 2005; Lue et al., 2009), and cell height measurments obtained by shear-force feedback topography have been combined with WFDI-based phase measurements (Edward et al., 2009). Another approach is to obtain the cell thickness by restraining the cell mechanically to a known thickness in the direction perpendicular to the image plane. This can be performed, for example, by

attaching another coverslip to the sample (Kemper et al., 2006) or using a dedicated microchannel device (Lue et al., 2006). This method, however, applies pressure to the cell and might disturb the behavior of the cell or affect the phenomena of interest. Kemper et al. (2007), Kemmler et al. (2007), and Tychinsky et al. (2008) have shown that for cells of a known uniform shape in suspension, the transverse viewable area of the cell can be used to evaluate cell thickness. For example, if the cell shape is a perfect sphere, its width is equal to its height. In all of these specific cases, the integral refractive index can be calculated using the phase profile obtained by WFDI since the cellular thickness is known.

4. Whole-cell-analysis based on WFDI phase profiles

In this section, we show that the WFDI-based phase profiles are useful for quantitative analysis of cells, even in cases where decoupling of thickness and refractive index is not possible or desired. This typically happens for highly-dynamic heterogeneous-refractive-index cells, such as cardiomyocytes (heart muscle cells). By coordinated contraction, these cells control blood flow through the blood vessels of the circulatory system. The dynamic behavior of cardiomyocytes is characterized by a rapid contraction of the cell followed by restoration to equilibrium. Contrary to cells with homogenous refractive index, cardiomyocytes contain organelles with varying refractive indices distributed across the cell interior. These mainly include myofibrils of highly organized sarcomeric arrays of myosin and actin, nuclei, and mitochondria. Using confocal dual-channel fluorescence microscopy, we have demonstrated that the cardiomyocyte organelles of different refractive indices are in motion during the entire beating cycle of the cell (Shaked et al., 2010 a). For this reason, it is not possible to accurately decouple refractive index from thickness using the phase-measurement of the entire cardiomyocyte obtained only from single-exposure WFDI. Furthermore, alternative approaches described previously that require more than one exposure (e.g. tomographic scanning or medium-exchange differential measurements; see Section 3) can result in loss of dynamic information when recording these cells due to their rapid dynamic nature. This limitation precludes calculating the cell thickness profiles from the phase measurements obtained by single-exposure WFDI during the cell beating cycle. In spite of this fact, we have shown that the dynamic WFDI-based phase profiles of the whole cell are still useful for numerical analysis of the cells (Shaked et al., 2010 a). This has been done by identifying certain numerical parameters that quantify specific processes of interest to cell biologists. We have validated the utility of the proposed parameters by showing they are sensitive enough to detect modification of cardiomyocyte contraction dynamics due to temperature change.

In order to numerically quantify the dynamic phase profile of the cells, without the need to extract the thickness profile, we first define the phase-average displacement (PAD) as follows (Shaked et al., 2010 a):

$$\Delta\varphi_t(x,y) = \varphi_t(x,y) - \varphi_0(x,y)\,, \tag{10}$$

where $\varphi_t(x,y)$ is the spatially varying phase at time point t, and $\varphi_0(x,y)$ is the spatially varying phase at the resting time point of the cell; if such a time point is not known, $\varphi_0(x,y)$ is defined as the time average of the entire phase-profile $\varphi_0(x,y) = \langle \varphi_t(x,y) \rangle_t$. Using Eq. (10), we define the positive and negative mean-square phase-average displacements (MS-PAD+ and MS-PAD–, respectively) as follows:

$$\Delta\varphi_{MS}^{+}(x,y)=\left\langle\left(\Delta\varphi_t(x,y)\right)^2:\Delta\varphi_t(x,y)\geq 0\right\rangle_t,$$
$$\Delta\varphi_{MS}^{-}(x,y)=\left\langle\left(\Delta\varphi_t(x,y)\right)^2:\Delta\varphi_t(x,y)<0\right\rangle_t, \tag{11}$$

and the spectral-domain MS-PAD as follows:

$$\Delta\varphi_{MS}(f_x,f_y)=\left\langle\left|\Delta\varphi_t(f_x,f_y)\right|^2\right\rangle_t, \tag{12}$$

where $\Delta\varphi_t(f_x,f_y)$ is obtained by a two-dimensional spatial Fourier transform of $\Delta\varphi_t(x,y)$. Using Eqs. (11) and (12), we define the following parameters to describe the MS-PAD global contributions:

$$\eta_1^{+}=\sqrt{\left\langle\Delta\varphi_{MS}^{+}(x,y)\right\rangle_{(x,y)}},$$
$$\eta_1^{-}=\sqrt{\left\langle\Delta\varphi_{MS}^{-}(x,y)\right\rangle_{(x,y)}}, \tag{13}$$
$$\eta_2=\sqrt{\left\langle\Delta\varphi_{MS}(f_x,f_y)\right\rangle_{(f_x,f_y)}},$$

where $\langle\bullet\rangle_{(x,y)}$ and $\langle\bullet\rangle_{(f_x,f_y)}$ define an area averaging.

Let us also define the phase instantaneous displacement (PID) as follows:

$$\Delta\varphi_{t,\tau}(x,y)=\varphi_{t+\tau}(x,y)-\varphi_t(x,y). \tag{14}$$

where τ defines the time duration between time point t and time point $t+\tau$. Using Eq. (14), we define the positive and negative mean-square phase instantaneous displacements (MS-PID+ and MS-PID–, respectively) as follows:

$$\Delta\varphi_{MS,\tau}^{+}(x,y)=\left\langle\left(\Delta\varphi_{t,\tau}(x,y)\right)^2:\Delta\varphi_{t,\tau}(x,y)\geq 0\right\rangle_t,$$
$$\Delta\varphi_{MS,\tau}^{-}(x,y)=\left\langle\left(\Delta\varphi_{t,\tau}(x,y)\right)^2:\Delta\varphi_{t,\tau}(x,y)<0\right\rangle_t, \tag{15}$$

as well as the spectral-domain MS-PID as follows:

$$\Delta\varphi_{MS,\tau}(f_x,f_y)=\left\langle\left|\Delta\varphi_{t,\tau}(f_x,f_y)\right|^2\right\rangle_t, \tag{16}$$

where $\Delta\varphi_{t,\tau}(f_x,f_y)$ is obtained by a spatial Fourier transform of $\Delta\varphi_{t,\tau}(x,y)$. By using Eqs. (15) and (16), we define parameters describing the MS-PID global contributions:

$$\gamma_{1,\tau}^{+}=\sqrt{\left\langle\Delta\varphi_{MS,\tau}^{+}(x,y)\right\rangle_{(x,y)}},$$
$$\gamma_{1,\tau}^{-}=\sqrt{\left\langle\Delta\varphi_{MS,\tau}^{-}(x,y)\right\rangle_{(x,y)}}, \tag{17}$$
$$\gamma_{2,\tau}=\sqrt{\left\langle\Delta\varphi_{MS,\tau}(f_x,f_y)\right\rangle_{(f_x,f_y)}}.$$

As the cell phase profile is strongly associated with its dry mass (Barer, 1952; Popescu et al., 2008 b; Rappaz et al., 2009), the parameters defined above are associated with motion of different intracellular structures including organelles. For example, the spectral-domain MS-PID has been used to describe cancer cell dynamics (Popescu et al., 2008 b). Note that all the parameters defined above are based on the entire dynamic phase profile, without the need to first extract the physical thickness profile.

The analysis tools described above are sensitive enough to detect the subtle changes in the dynamic phase profile of a beating cardiomyocyte (Shaked et al., 2010 a). Figures 4(a) and 4(e) compare the phase profiles of a cardiomyocyte during a single beating cycle at 30°C and 23°C, respectively. The cell in Fig. 4(e) show more motion along a greater portion of its length in comparison to the cell shown in Fig. 4(a), especially in the recovery stage (defined as the time interval between the point of maximum stretch of the cell and the point when the cell returned to the resting stage). The relatively slow recovery phase observed at lower temperatures is consistent with temperature-induced inhibition of calcium-regulated contraction, as discussed at the end of this section. The dynamic differences during the beating cycle of the same cell at 30°C in comparison to 23°C are more obvious from the PAD and PID profiles shown in Figs. 4(b-d,f-h) (also see Media 4 in Shaked et al., 2010 a). As seen in Figs. 4(b,f), the PAD profiles of cardiomyocytes provide a means of tracking the differential changes in the current WFDI phase profile compared to the associated phase profile in the cell resting point (defined by Eq. (10)), which reveals the dry-mass movement inside the cell. Thus the PAD profiles can be used to study cell function during the beating cycle. Furthermore, the global contribution of the dynamic PAD profiles characterizes the entire beating cell cycle and is the basis for the MS-PAD profiles, which are described by the single-value η parameters. As can be seen in Figs. 4(c,d,g,h), the PID profiles give an indication of the instantaneous movement of dry mass in the cell associated with organelles of different sizes over different time periods during the cell beating cycle, as defined by the time parameter τ. The subtraction operation defined by Eq. (14) creates a differential measurement between the current phase profile and a previous phase profile that is time-shifted by τ. Phase contributions from this previous frame are thus canceled and the uncorrelated regions between the two frames are revealed. The MS-PID profiles are calculated based on the dynamic PID profiles, yielding the single-valued γ parameters characterizing the cell over various time periods during the experiment.

Figures 5(a,b) and (c,d) show the MS-PAD profiles obtained for the dynamic PAD profiles shown in Figs. 4(b) and (f) at 30°C and 23°C, respectively. These MS-PAD profiles were used to calculate the η parameters as defined by Eq. (4), and for this particular cell yielded $\eta_1^+ = 0.10998$ and $\eta_1^- = 0.10941$ at 30°C, and $\eta_1^+ = 0.10249$ and $\eta_1^- = 0.10251$ at 23°C. In a similar way, the associated spectral-domain PAD profile yielded $\eta_2 = 16.8186$ at 30°C and $\eta_2 = 16.1487$ at 23°C.

Figures 5(e,f) and (g,h) show the MS-PID profiles for $\tau = 8.3$ msec (single-frame separation at 120 fps) at 30°C and 23°C, respectively. Media 5 in Shaked et al. (2010 a) presents the associated dynamic MS-PID profiles as a function of the time parameter τ. Based on these dynamic MS-PID profiles and on the spectral domain MS-PID profile, we calculated the γ parameters as defined by Eq.(17). Figures 5(i-k) show the dependency of the various γ parameters on τ at the two temperature levels. As can be seen from these graphs, the difference between the two temperature levels is more pronounced for higher τ values than for lower τ values. This result is expected due to the fact that the change between the two temperature levels is more pronounced in the recovery phase of the cardiomyocyte beating cycle.

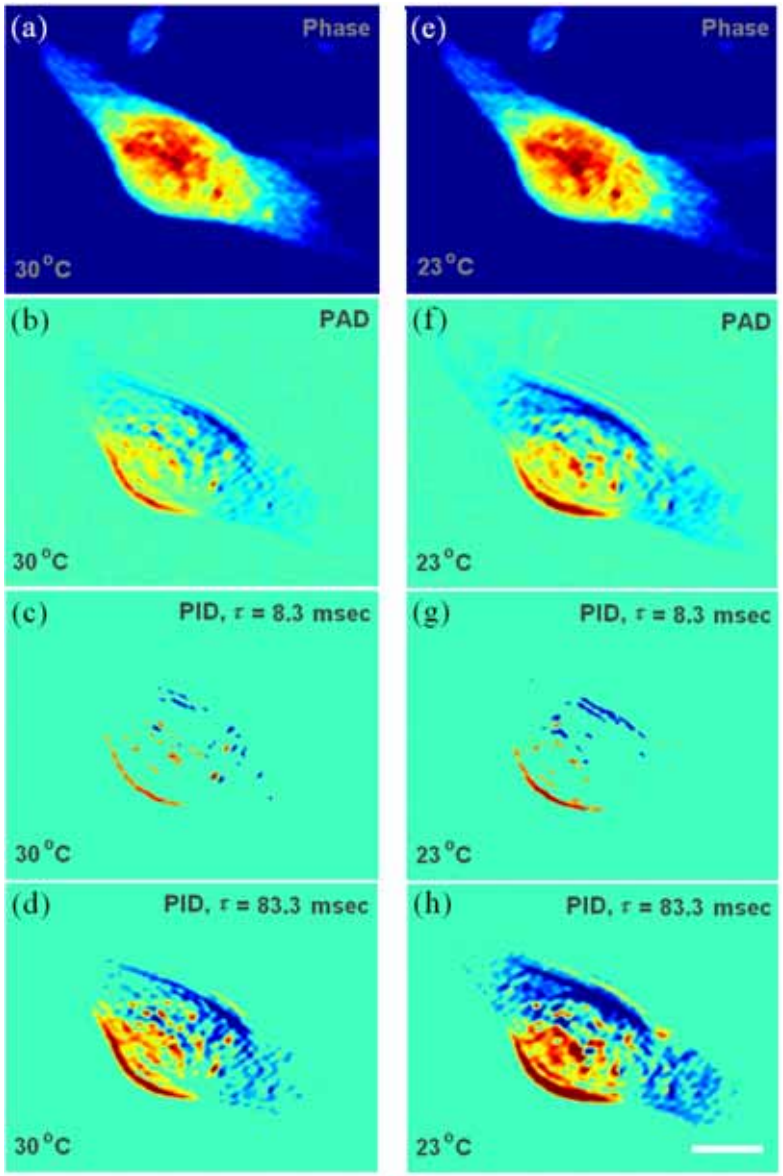

Fig. 4. Example of numerical analysis applied on a WFDI-based phase profile of a cardiomyocyte during beating at two different temperatures: (a-d) at 30°C, (e-h) at 23°C. (a,e) Phase profile; (b,f) PAD profile; (c,g) PID profile for τ = 8.3 msec (single-frame separation at 120 fps); (d,h) PID profile for τ = 83.3 msec (ten-frame separation at 120 fps). In (b-d,f-h): 'hot' colors represent positive values, 'cold' colors represent negative values, and cyan represents zeros. White horizontal scale bar represents 10 μm. Dynamics, 120 fps for 1 sec: see Media 4 in (Shaked et al., 2010 a).

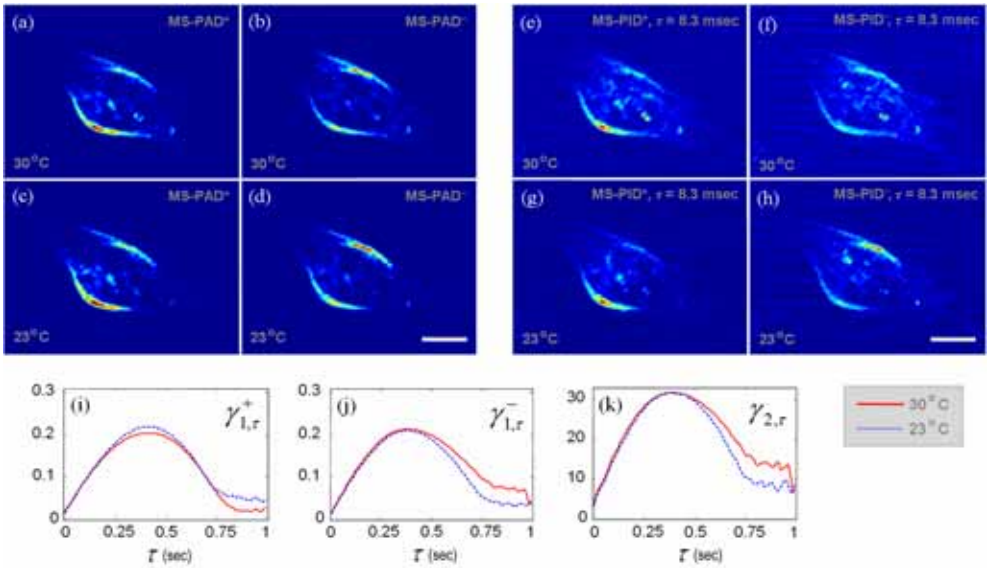

Fig. 5. Calculation of different numerical parameters based on the dynamic phase profiles shown in Fig. 4. (a-d) MS-PAD profiles (based on which the η parameters are defined): (a) MS-PAD+ at 30°C (which yields $\eta_1^+ = 0.10998$); (b) MS-PAD– at 30°C (which yields $\eta_1^- = 0.10941$); (c) MS-PAD+ at 23°C (which yields $\eta_1^+ = 0.10249$); (d) MS-PAD– at 23°C (which yields $\eta_1^- = 0.10251$). (e-h) MS-PID profiles for τ = 8.3 msec; varying τ: Media 5 in (Shaked et al., 2010 a): (e) MS-PID+ at 30°C; (f) MS-PID– at 30°C; (g) MS-PID+ at 23°C; (h) MS-PID– at 23°C. (i-k) Graphs showing the dependency of the γ parameters on τ. Solid red lines represent the measurements done at 30°C. Dashed blue lines represent the measurements done at 23°C. (i) $\gamma^{+}_{1,\tau}$ (which is based on MS-PID+); (j) $\gamma^{-}_{1,\tau}$ (which is based on MS-PID–); (k) $\gamma_{2,\tau}$ (which is based on the spectral-domain MS-PID). The white horizontal scale bars represent 10 μm. (Shaked et al., 2010 a).

The numerical analysis described above was performed on the WFDI phase profiles of 18 individual cardiomyocytes at 30°C (Shaked et al. 2010 a). The values obtained for each of the γ and η parameters were averaged over 3-4 beating cycles and normalized by the viewable area of the cell. Afterwards, the experiments were repeated at 23°C. Figure 6 summarizes the results obtained. Statistical significance between the two groups of cells (at 30°C and at 23°C) was seen for all γ and η parameters as indicated by low p-values, which were calculated by the two-sided Wilcoxon rank-sum test (Conover, 1999). These results demonstrate that these unique whole-cell-based numerical parameters can be used to discriminate between different dynamic behaviors of cardiomyocytes, and thus can be used to quantitatively study dynamic phenomena in these cells.

As can also be seen in Fig, 6, there is an apparent advantage for using the negative parameters $\gamma^{-}_{1,\tau}$ for discriminating between the two groups of cells. Higher values in these parameters represent increased levels of MS-PID–. In the recovery phase of the cell, it is more likely to have more cell points with negative MS-PID than positive MS-PID, since the phase profile in the cell contractile region decreases. This implies that there is a larger influence of the ambient temperature on the recovery phase of the cell beating, as compared

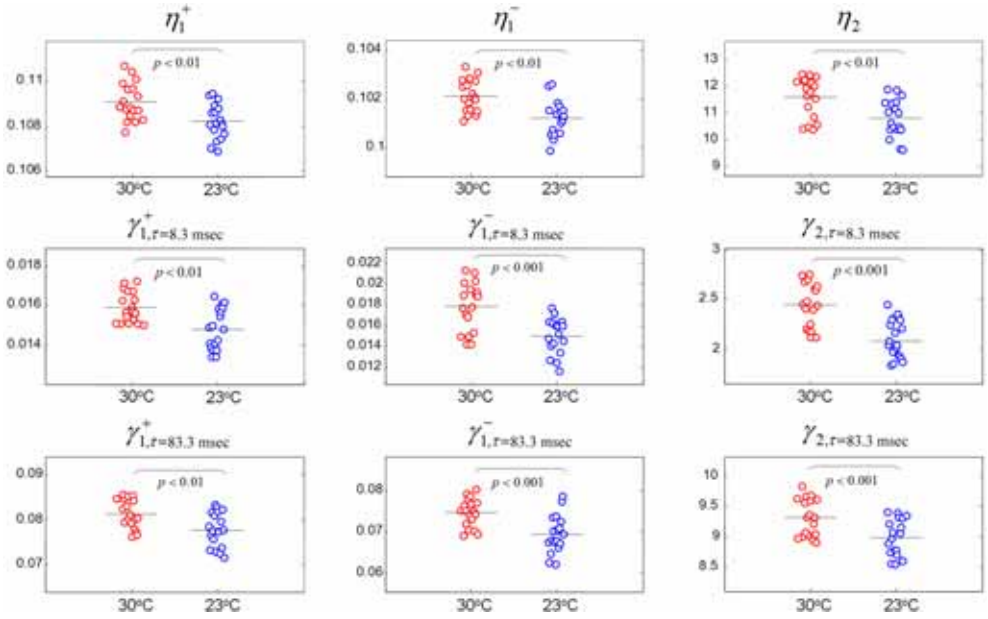

Fig. 6. Values of the γ and η parameters that are based on the whole-cell phase profiles, demonstrating that these parameters discriminate between cardiomyocytes beating at 30°C and 23°C (18 cells in each group, 3-4 beating cycles per each cell). Each circle represents a different cardiomyocyte, and the horizontal line at each group represents the average value for all cells in the group. (Shaked et al., 2010 a).

to the contraction phase. These results are supported by previous studies performed by other methods, where temperature had a profound effect on the biochemistry of contraction in the myocardium of the intact heart and in cardiomyocytes *in vitro* (Covell et al., 1966; Badeer, 1967; Engel et al., 1995; Fu et al., 2005).

The whole-cell analysis tools presented here capture intermediate events associated with dry mass movement over different time scales during the cardiomyocyte beating cycle. These intermediate events cannot be well discriminated by directly visualizing the dynamic phase profiles of the cell. In contrast, the single-valued η and γ parameters can uniquely characterize cell function, as demonstrated for temperature change. We believe that these numerical tools will also be useful for analyzing various fast dynamic behaviors in other biological cells, including intracellular and extracellular membrane fluctuations and reorganization of the cell cytoskeleton. More details on this stubject can be found in (Shaked et al., 2010 a).

5. Conclusion

We have started by presenting the principles of WFDI phase microscopy for quantitative holgoraphic imaging of biological cells. After illustrating the transmissive optical geometry employed, we reviewed methods of recovering phase information from the captured interferometric intensity pattern (which is the digital hologram of the sample). Phase

profiles can then be converted to OPD, which contain the specimen coupled refractive index and physical thickness.

We have also discussed methods of calculating meaningful biological parameters from the OPD measurement. While it is straightforward to decouple physical thickness from refractive index in homogeneous samples where one of the two parameters can be determined ahead of time or taken from literature values and assumed constant, parameters such as dry mass, relative area, and relative volume can be calculated even for heterogeneous samples without decoupling physical thickness and refractive index. We demonstrated the utility of this technique by analyzing individual articular chondrocytes under hypoosmotic loading and characterized dynamic changes in the dry mass, area, and relative volume. Several other systems made use of multiple measurements at varying angular projections, immersion media, or wavelengths in an attempt to decouple refractive index from physical thickness; however all of these techniques trade off system complexity and temporal resolution in order to extract these parameters.

Finally, we presented whole-cell analysis that makes use of differential phase profiles referenced to either an initial physiological state (phase-average displacement, PAD) or a finite time delay (phase-instantaneous displacement, PID). Examining the PAD and PID over the course of a dynamic experiment provides information about the motion of intracellular organelles. Furthermore, analysis of global contribution parameters γ and η has been shown to be effective at discriminating dynamic cellular behavior as influenced by environmental variables such as temperature.

The development of WFDI phase microscopy has introduced a variety of optical techniques for obtaining label-free quantitative information about the structure of cells. While phase contrast and DIC microscopy have previously utilized OPDs induced by cellular structures to provide relative image contrast and qualitative measurements, quantification of phase profiles by WFDI represents a major development that allows more rigorous studies of cellular behavior over time. Furthermore, WFDI phase microscopy can in many cases obviate the need for exogenous contrast agents such as fluorophores whose drawbacks may include photobleaching over time, cytotoxicity, and potential modification of intracellular behavior in response to the fluorophore or bound antibody. While WFDI is a whole-cell hologaphic approach and thus does not provide contrast arising from molecular specificity, it is a label-free quantitative technology that complements labeled-based (e.g. fluorescence) imaging for investigating and quantifying cellular dynamics.

WFDI phase microscopy has been shown to be highly effective for high speed cellular dynamics studies without the need for special sample preparation. The presented set of holographic techniques has significant potential applications for characterization of various cellular phenomena and disease conditions.

6. Acknowledgments

This work was supported by National Science Foundation (NSF) grant CBET-0651622. N.T.S. greatly acknowledges the support of the Bikura Postdoctoral Fellowship from Israel.

7. References

Badeer, H. S. (1967) Effect of hypothermia on the contractile 'capacity' of the myocardium, *Journal of Thoracic and Cardiovascular Surgery* 53, 5, (May 1967) 651-656

Barer, R. (1952) Interference microscopy and mass determination, *Nature* 169, 4296, (March 1952) 366-367

Charrière, F.; Marian, A.; Montfort, F.; Kuehn, J.; Colomb, T.; Cuche, E.; Marquet, P. & Depeursinge, C. (2006) Cell refractive index tomography by digital holographic microscopy, *Opt. Lett.* 31, 2, (January 2006) 178-180

Choi, W.; Fang-Yen, C.; Badizadegan, K.; Oh, S.; Lue, N.; Dasari, R.R. & Feld, M. S. (2007) Tomographic phase microscopy, *Nature Methods* 4, (August 2007) 717-719

Conover, W. J. (1999) *Practical Nonparametric Statistics*, 3rd Edition, John Wiley, pp. 271-276.

Covell, J.W.; Ross Jr., J.; Sonnenblick, E. H. & Braunwald, E. (1966) Comparison of the force-velocity relation and the ventricular function curve as measures of the contractile state of the intact heart, *Circulation Research* 19, (March 1966) 364-372

Cuche, E.; Marquet, P. & Depeursinge, C. (1999) Simultaneous amplitude-contrast and quantitative phase-contrast microscopy by numerical reconstruction of Fresnel off-axis holograms, *Appl. Opt.* 38, 34, (December 1999) 6994-7001

Curl, C.L.; Bellair, C.J.; Harris, T.; Allman, B.E.; Harris, P.J.; Stewart, A.G.; Roberts, A.; Nugent, K.A. & Delbridge, L.M. (2005) Refractive index measurement in viable cells using quantitative phase-amplitude microscopy and confocal microscopy, *Cytometry* 65, 1, (May 2005) 88-92

Edward, K.; Farahi, F. & Hocken, R. (2009) Hybrid shear force feedback/scanning quantitative phase microscopy applied to subsurface imaging, *Opt. Express* 17, 21, (October 2009) 18408-18418

Engel, J.; Sowerby, A.J.; Finch, S.A.; Fechner, M. & Stier, A. (1995) Temperature dependence of Ca^{2+} wave properties in cardiomyocytes: implications for the mechanism of autocatalytic Ca^{2+} release in wave propagation, *Biophysical J.* 68, 1, (January 1995) 40-45

Fu, Y.; Zhang, G.-Q.; Hao, X.-M.; Wu, C.-H.; Chai, Z. & Wang, S.-Q. (2005) Temperature dependence and thermodynamic properties of Ca^{2+} sparks in rat cardiomyocytes, *Biophysical J.* 89, 4, (October 2005) 2533-2541

Ikeda, T.; Popescu, G.; Dasari, R.R. & Feld, M.S. (2005) Hilbert phase microscopy for investigating fast dynamics in transparent systems, *Opt. Lett.* 30, 10, (May 2005) 1165-1167

Kemmler, M.; Fratz, M.; Giel, D.; Saum, N.; Brandenburg, A. & Hoffmann, C. (2007) Non-invasive time-dependent cytometry monitoring by digital holography, *J. Biomed. Opt.* 12, 6, (Nov-Dec 2006) 064002

Kemper, B.; Kosmeier, S.; Langehanenberg, P.; von Bally, G.; Bredebusch, I.; Domschke, W. & Schnekenburger, J. (2007) Integral refractive index determination of living suspension cells by multifocus digital holographic phase contrast microscopy, *J. Biomed. Opt.* 12, 5, (Sept-Oct 2007) 054009

Kemper, B.; Carl, D.; Schnekenburger, J.; Bredebusch, I.; Schafer, M.; Domschke, W. & von Bally, G. (2006) Investigation of living pancreas tumor cells by digital holographic microscopy, *J. Biomed. Opt.* 11, 3, (May-Jun 2006) 34005

Lue, N.; Choi, W.; Popescu, G.; Yaqoob, Z.; Badizadegan, K.; Dasari, R.R. & Feld, M.S. (2009) Live cell refractometry using Hilbert phase microscopy and confocal reflectance microscopy, *Journal of Physical Chemistry A*, 113, (October 2009) 13327-13330

Lue, N.; Popescu, G.; Ikeda, T.; Dasari, R.R.; Badizadegan, K. & Feld, M.S. (2006) Live cell refractometry using microfluidic devices, *Opt. Lett.* 31, 18, (September 2006) 2759-2761

Marquet, P.; Rappaz, B.; Magistretti, P.J.; Cuche, E.; Emery, Y.; Colomb, T. & Depeursinge, C. (2005) Digital holographic microscopy: a noninvasive contrast imaging technique allowing quantitative visualization of living cells with subwavelength axial accuracy, *Opt. Lett.* 30, 5, (March 2005) 468-470

Park, Y.K.; Diez-Silva, M.; Fu, D.; Popescu, G.; Choi, W.; Barman, I.; Suresh, S. & Feld, M.S. (2010) Static and dynamic light scattering of healthy and malaria-parasite invaded red blood cells, *Journal of Biomedical Optics Letters* 15, 2, (March-April 2010) 020506

Park, Y. K.; Diez-Silva, M.; Popescu, G.; Lykorafitis, G.; Choi, W.; Feld, M.S. & Suresh, S. (2008) Refractive index maps and membrane dynamics of human red blood cells parasitized by Plasmodium falciparum, *Proc. Natl. Acad. Sci. USA. (PNAS)* 105, (2008) 13730

Park, Y.K.; Popescu, G.; Badizadegan, K.; Dasari, R.R. & Feld, M.S. (2006) Diffraction phase and fluorescence microscopy, *Opt. Express* 14, 18, (September 2006) 8263-8268

Popescu, G.; Park, Y.K.; Choi, W.; Dasari, R.R.; Feld, M.S. & Badizadegan, K. (2008 a) Imaging red blood cell dynamics by quantitative phase microscopy, *Blood Cells, Molecules and Diseases* 41, 1, (July-Aug 2008) 10-16

Popescu, G.; Park, Y.K.; Lue, N.; Best-Popescu, C.A.; Deflores, L.; Dasari, R.R.; Feld, M.S. & Badizadegan, K. (2008 b) Optical imaging of cell mass and growth dynamics, *The American Journal of Physiology - Cell Physiology* 295, (June 2008) C538-C544

Popescu, G.; Ikeda, T.; Badizadegan, K.; Dasari, R.R. & Feld, M.S. (2005) Erythrocyte structure and dynamics quantified by Hilbert phase microscopy, *J. Biomed. Opt. Lett.* 10, (2005) 060503

Rappaz, B.; Cano, E.; Colomb, T.; Kühn, J.; Simanis, V.; Depeursinge, C.; Magistretti, P.J. & Marquet, P. (2009) Noninvasive characterization of the fission yeast cell cycle by monitoring dry mass with digital holographic microscopy, *J. Biomed. Opt.* 14, 3, (May-June 2009) 034049

Rappaz, B.; Barbul, A.; Emery, Y.; Korenstein, R.; Depeursinge, C.; Magistretti, P.J. & Marquet, P. (2008 a) Comparative study of human erythrocytes by digital holographic microscopy, confocal microscopy, and impedance volume analyzer, *Cytometry A.* 73, 10, (October 2008) 895-903

Rappaz, B.; Charrière, F.; Depeursinge, C.; Magistretti, P.J. & Marquet, P. (2008 b) Simultaneous cell morphometry and refractive index measurement with dual-wavelength digital holographic microscopy and dye-enhanced dispersion of perfusion medium, *Opt. Lett.* 33, 7, (April 2008) 744-746

Rappaz, B.; Marquet, P.; Cuche, E.; Emery, Y.; Depeursinge, C. & Magistretti, P. (2005) Measurement of the integral refractive index and dynamic cell morphometry of living cells with digital holographic microscopy, *Opt. Express* 13, 23, (November 2005) 9361-9373

Shaked, N. T.; Satterwhite, L.L.; Bursac, N. & Wax, A. (2010 a) Whole-cell-analysis of live cardiomyocytes using wide-field interferometric phase microscopy, *Biomedical Optics Express* 1, 2, (September 2010) 706-719

Shaked, N. T.; Zhu, Y.; Badie, N.; Bursac, N. & Wax, A. (2010 b) Reflective interferometric chamber for quantitative phase imaging of biological sample dynamics, *J. of Biomed. Opt. Lett.* 15, 3, (May-June 2010) 030503

Shaked, N. T.; Newpher, T.M.; Ehlers, M.D. & Wax, A. (2010 c) Parallel on-axis holographic phase microscopy of biological cells and unicellular microorganism dynamics, *Appl. Opt.* 49, 15, (May 2010) 2872-2878

Shaked, N. T.; Finan, J.D.; Guilak, F. & Wax, A. (2010 d) Quantitative phase microscopy of articular chondrocyte dynamics by wide-field digital interferometry, *J. Biomed. Opt. Lett.* 15, 1, (Jan-Feb 2010) 010505

Shaked, N. T.; Zhu, Y.; Rinehart, M.T. & Wax, A. (2009 a) Two-step-only phase-shifting interferometry with optimized detector bandwidth for microscopy of live cells, *Opt. Express* 17, 18, (August 2009) 15585-15591

Shaked, N. T.; Rinehart, M.T. & Wax, A. (2009 b) Dual-interference-channel quantitative-phase microscopy of live cell dynamics, *Opt. Lett.* 34, 6, (March 2009) 767-769

Tychinsky, V.P.; Kretushev, A.V.; Klemyashov, I.V.; Vyshenskaya, T.V.; Filippova, N.A.; Raikhlin, N.T. & Shtil, A.A. (2008) Quantitative real-time analysis of nucleolar stress by coherent phase microscopy, *J. Biomed. Opt.* 13, 6, (Nov-Dec 2008) 064032